Microstructure Distribution in 17-4 PH Martensitic Steel Produced by Selective Laser Melting

IGOR VYSOTSKIY, SERGEY MALOPHEYEV, IVAN ZUIKO, SERGEY MIRONOV, and RUSTAM KAIBYSHEV

In this work, electron backscatter diffraction (EBSD) was applied to investigate the microstructure distribution within the selective-laser-melted 17-4 PH martensitic steel. The volume fraction of the δ-ferrite was found to decrease in the building direction. This effect was attributed to the decrease in the cooling rate, which promoted the δ-ferrite $\rightarrow$ austenite $\rightarrow$ α-martensite transformation sequence.

https://doi.org/10.1007/s11661-022-06829-5

DUE to the attractive combination of service properties, precipitation hardening (PH) martensitic steels are widely used in nuclear, aerospace, marine, and chemical industries. However, the poor workability of these materials restricts their application for the fabrication of complex-shaped products. Additive manufacturing technology and, particularly, the selective laser melting (SLM) technique offer a great opportunity to bypass this problem.

The SLM approach involves the incremental, layer-by-layer melting and fusion of a metal powder by a laser beam according to an appropriate computer model.[1] Due to the specific character of the SLM process, the manufactured material experiences a complex thermal history that involves an extremely high cooling rate and a repetitive melting-to-solidification sequence. In martensitic steels, this often results in a complex phase structure composed of δ-ferrite, austenite, and α-martensite [*e.g.*, References 2–13].

Assuming that microstructure evolution during SLM is mainly governed by solidification and subsequent cooling phenomena, it is thought that cooling rate plays one of the key roles in this process. Due to the rapid heat sink into the backing plate, the cooling rate should be highest at the bottom part of the manufactured material, but then it may perhaps decrease along the building direction. If so, this may result in an inhomogeneous microstructure distribution in the SLM-produced samples. To the best of the authors' knowledge, this issue has not been examined in martensitic steels so far. Therefore, it was the purpose of the present work.

IGOR VYSOTSKIY, SERGEY MALOPHEYEV, IVAN ZUIKO, SERGEY MIRONOV, and RUSTAM KAIBYSHEV are with the Belgorod National Research University, Pobeda 85, Belgorod 308015, Russia. Contact e-mail: mironov@bsu.edu.ru
Manuscript submitted June 21, 2022; accepted September 10, 2022.

The material used in the present investigation was 17-4 PH martensitic steel with a nominal chemical composition (in wt pct) of 15–17 pct Cr, 3–5 pct Ni, 3–5 pct Cu, 1 pct Mn, 1 pct Si, 0.15–0.45 pct Nb, and the balance Fe. This is a typical PH martensitic steel that is widely used in industry. The material was supplied as nitrogen-atomized powder by 3D Systems, Inc. The SLM process was conducted using a ProX DMP 200 machine (3D Systems Inc.). The manufacturer-recommended processing parameters were used, including the laser power of 240 W, the laser-scanning speed of 2500 mm/s, a hatch distance of 50 μm, and a layer thickness of 30 μm. The typical convention for SLM geometry was adopted, where BD was the build direction, SD was the laser-scanning direction, and RD was the motion direction of the powder distribution roller. A cuboidal-shaped sample with dimensions 10 $\times$ 10 $\times$ 20 mm^3 (SD $\times$ RD $\times$ BD) was built in a nitrogen atmosphere using a parallel scan strategy with alternating scan directions.

Microstructural observations were conducted using electron backscatter diffraction (EBSD) in the longitudinal (RD $\times$ BD) cross-section plane. The appropriate surface finish was obtained using conventional metallographic techniques followed by long-term (24-h) vibratory polishing with a colloidal silica suspension. EBSD analysis was performed employing an FEI Quanta 600 field-emission-gun scanning electron microscope (SEM) equipped with TSL OIM™ software and operated at 20 kV. To investigate the throughout-thickness microstructure distribution within the manufactured sample, three particular locations were examined, viz., its bottom, central, and top parts. To provide thorough insight into the microstructure, two EBSD maps were acquired in each case: a low-resolution one (a scan step size of 0.5 μm) and a high-resolution one (a scan step size of 0.2 μm). The total statistics of EBSD measurements are summarized in supplementary Table S-1 (refer

Published online: 27 September 2022

the electronic supplementary material). During EBSD, the δ-ferrite and α-martensite were indexed as the generic body-centered-cubic (BCC) phase, while the austenite was indexed as the generic face-centered-cubic (FCC) phase. To improve the fidelity of EBSD data, all fine grains comprising one or two pixels were automatically removed (“cleaned”) from EBSD maps using the standard grain-dilation option of the EBSD software.

The particular EBSD characteristic, the image-quality (IQ) index, was used for microstructural analysis. The IQ index characterizes the sharpness of the Kikuchi bands in a digitized diffraction pattern and serves as a qualitative measure of stored energy. In steels, microstructural domains with relatively high and low IQ often represent ferrite and martensite, respectively. In the present work, two types of representation of IQ data were used, *i.e.*, grayscale and color. The grayscale maps resemble the typical appearance of microstructure in SEM, whereas the color-coded IQ maps are highly sensitive to microstructural variations.

EBSD observations showed that the microstructures that evolved in the bottom, central, and top parts of the manufactured sample were broadly similar to each other, at least in appearance. Hence, only EBSD maps taken from the center are shown in Figure 1, while the remaining results are provided in Supplementary Figures S-1 and S-2.

In all cases, the microstructures produced during SLM comprised a complex mixture of BCC and FCC constituents (Figure 1). Moreover, the BCC constituent appeared to consist of two distinct components, coarse-grained and fine-grained ones (Figure 1).

The *coarse-grained* BCC component was characterized by columnar-shaped grains and relatively bright IQ contrast (*i.e.*, the low stored energy). Hence, this microstructural constituent was presumably δ-ferrite. Remarkably, the ferrite grains were not distributed uniformly throughout the microstructure but tended to cluster in local areas. Those presumably represented the local molten pools produced during SLM. The preservation of δ-ferrite in the final microstructure evidenced the extremely high cooling rate.

It is worth noting that the average depth of the molten pools (~ 50 μm, Figure 1(b)) essentially exceeded the thickness of the powder layer (≈30 μm). This observation suggests that the manufactured material experienced at least two melting-to-solidification cycles during SLM.

On the other hand, the *fine-grained* BCC component exhibited the lath-shaped morphology and comparatively dark IQ contrast (*i.e.*, the high stored energy), as shown in Figure 1. Considering these attributes, this microstructural constituent was likely α-martensite. Importantly, the martensitic phase was arranged in-between the ferrite clusters, *i.e.*, virtually near the outer edges of the former molten pools. These areas should be most influenced by thermal cycling during SLM, and therefore the cooling rate there may be low enough for realization of the δ-ferrite $\rightarrow$ austenite $\rightarrow$ α-martensite transformation sequence.

The FCC constituent was clearly austenite. Notably, the relatively coarse austenitic particles were found within the ferrite domains, typically at the ferrite grain boundaries (Figure 1(b)). Hence, these particles likely originated from the δ-ferrite $\rightarrow$ austenite phase transformation during material cooling. On the other hand, the comparatively fine austenitic particles were preferentially concentrated within the martensitic-rich areas (Figure 1(b)). Therefore, these may be produced (at least partially) due to the α-martensite $\rightarrow$ austenite reversion during the SLM-induced thermal cycling, as has been suggested by Zai *et al.*[14].

The black areas seen in the IQ EBSD maps were also worthy of note (Figure 1). These presumably represented residual porosity inherent to the SLM process.

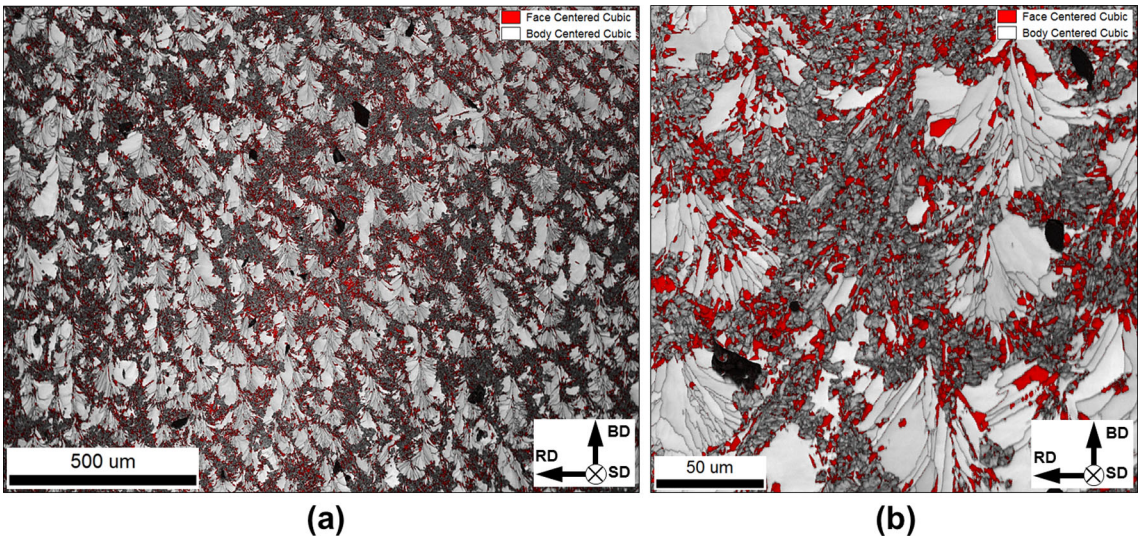

Fig. 1—The EBSD IQ maps with overlaid phase maps taken from the central part of manufactured sample: (*a*) low-resolution (overview) map and (*b*) high-resolution map. The phase color code is given in the top right corner of the maps. Black areas represent porosity (Color figure online).

Thus, in accordance with expectations, the SLM-induced microstructure consisted of a complex mixture of δ-ferrite, austenite, and α-martensite. While the detection of the austenitic phase was comparatively easy, the unbiased discrimination of δ-ferrite and α-martensite was challenging. This is primarily due to the relatively small difference between the crystal structures of the two latter phases, which is hard to distinguish using the commercially available EBSD systems.

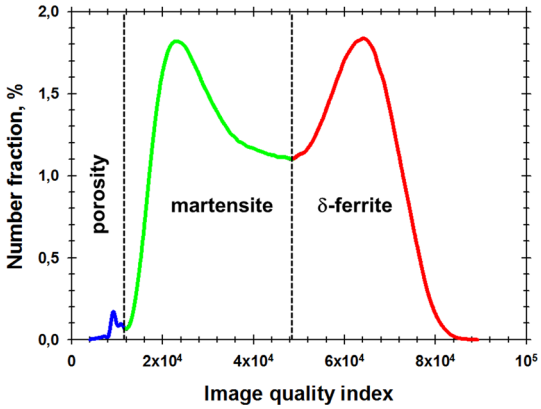

Figure 2—Distribution of IQ index for BCC phase derived from the low-resolution EBSD map in Fig. 1(a).

To overcome this problem, a number of approaches have been elaborated recently [*e.g.*, References 15–19]. Those are typically based on a presumption of a significant difference in the stored energy between ferrite and martensite. Hence, the related EBSD characteristics (usually the IQ index) should exhibit a bimodal distribution. The approaches imply the determination of a threshold IQ, which delimitates these two phases.

The IQ distributions derived from the BCC component are shown in Figure 2 and supplementary Figure S-3. In all cases, the distributions exhibited three distinct peaks; for clarity, these were highlighted by blue, green, and red. From the graphs, the threshold IQ indexes were determined (broken lines in Figure 2 and supplementary Figure S-3).

Based on the determined thresholds, EBSD data were partitioned on microstructural constituents, as shown in Figure 3 and supplementary Figures S-4 and S-5. For illustrative purposes, the color-coded IQ map was used for this purpose (Figure 3(a)) because of its particular sensitivity to microstructural variations.

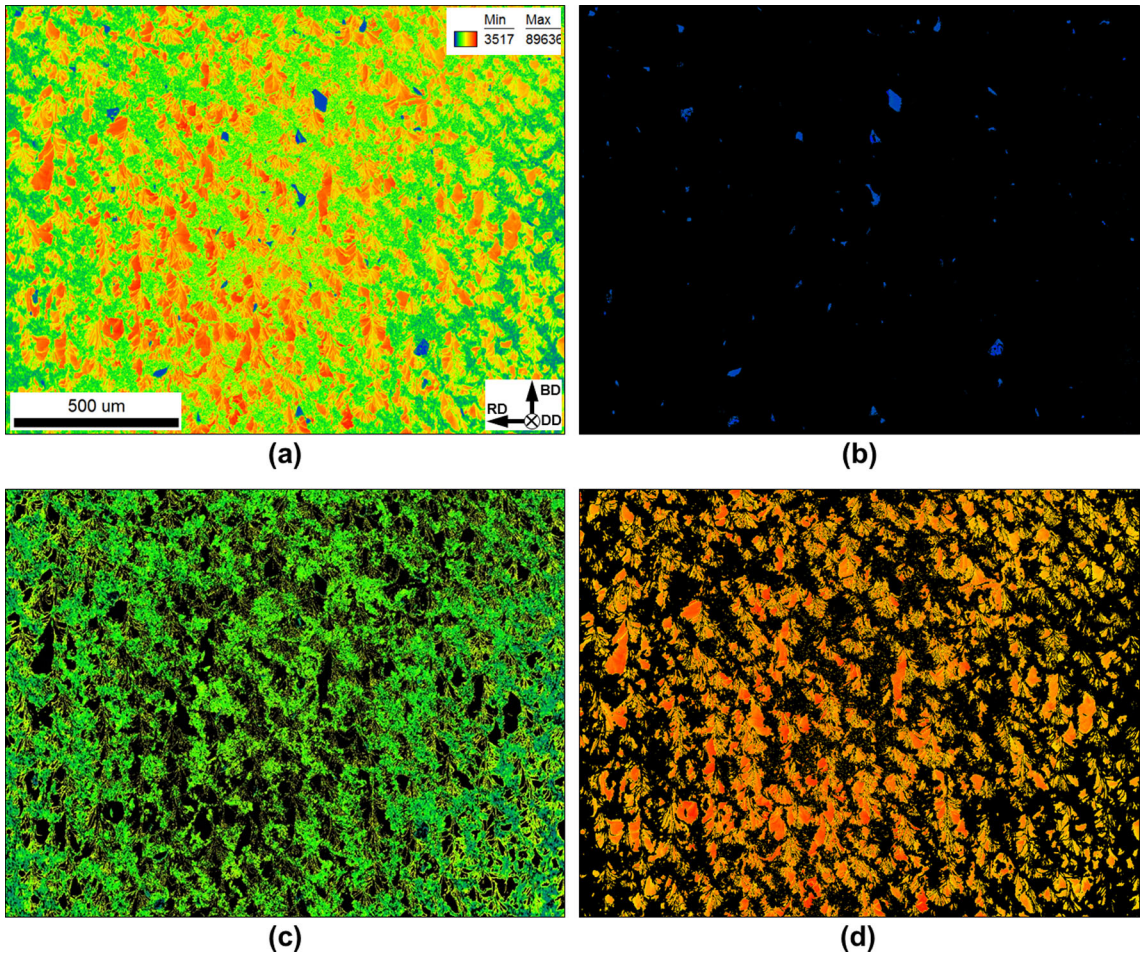

Figure 3—EBSD partitioning of microstructure: (*a*) the entire color-coded IQ map, (*b*) porosity, (*c*) martensitic phase, and (*d*) δ-ferritic phase. The color code for IQ for all maps is given in the top right corner of (a) (Color figure online).

Table I. The Variation of the Phase Volume Fraction Along the Building Direction

Location	Volume Fraction, Pct		
	δ-Ferrite	Austenite	α-Martensite
Bottom	37.4	18.9	43.2
Center	38.8	17.6	43.0
Top	26.0	18.3	55.3

From the partitioning, it was found that the data points with the lowest IQ (the blue-colored peak in Figure 2) reflected porosity (compare Figures 3(a) and (b)). On the other hand, the intermediate IQ peak (*i.e.*, the green-colored one in Figure 2) was associated with the fine-grained microstructural component (compare Figures 3(a) and (c)), and thus presumably represented the α-martensite. Finally, the EBSD data with the highest IQ (the red-colored peak in Figure 2) were linked to coarse columnar-shaped grains (compare Figures 3(a) and (d)), *i.e.*, the δ-ferrite.

In all cases, therefore, a good agreement between the magnitude of the IQ index and particular microstructural constituents was found. By using the above technique, the variation of the phase volume fractions along the building direction was examined (Table I). In the bottom and central parts of the manufactured sample, the phase content was found to be nearly the same. On the other hand, the martensite fraction in the top part of the sample increased at the expense of δ-ferrite.

To comprehend the latter observation, it is worth noticing that the preservation of δ-ferrite in SLM manufactured steels is usually attributed to an extremely high cooling rate [*e.g.*, Reference 11], which is believed to achieve ~ 10^6 °C/s. Hence, the observed decrease in the ferrite content implied an enhancement of the decomposition of this phase, thus virtually evidencing the decrease in cooling rate. This supports the initial idea of this work on the reduction of the cooling rate along the building direction of manufactured materials.

In this work, the microstructure distribution in the selective-laser-melted 17-4 PH steel was examined. To this end, extensive EBSD measurements were conducted at the bottom, mid-thickness, and upper sections of the as-built sample. In all cases, the produced microstructures comprised a complex mixture of δ-ferrite, austenite, and α-martensite. The preservation of δ-ferrite and austenite was attributed to the extremely high cooling rate intrinsic to the SLM process. On the other hand, the significant fraction of α-martensite was associated with thermal cycling, which is also inherent to SLM and may promote the decomposition of δ-ferrite and austenite at the outer edge of local molten pools.

Of particular importance was the observation that the volume fraction of the δ-ferrite phase was found to be relatively low near the upper part of the manufactured sample. This effect was attributed to the global decrease in the cooling rate, which enhanced the δ-ferrite → austenite → α-martensite transformation sequence.

All data included to this study are available upon request by contact with corresponding author.

The authors declare that they have no conflict of interest. This work was performed using the equipment of the Joint Research Center "Technology and Materials" at Belgorod National Research University (financial support from the Ministry of science and higher education of the Russian Federation under the Agreement No. 075-15-2021-690, the unique project identifier RF 2296.61321X0030). The authors are also grateful to Alexander Kalinenko for help with EBSD measurements.

SUPPLEMENTARY INFORMATION

The online version contains supplementary material available at https://doi.org/10.1007/s11661-022-06829-5.

REFERENCES

1. D.D. Gu, W. Meiners, K. Wissenbach, and R. Poprawe: *Int. Mater. Rev.*, 2012, vol. 57, pp. 133–64. https://doi.org/10.1179/1743280411Y.0000000014.
2. L.E. Murr, S.M. Gaytan, D.A. Ramirez, E. Martinez, J. Hernandez, K.N. Amato, P.W. Shindo, F.R. Medina, and R.B. Wicker: *J. Mat. Sci. Technol.*, 2012, vol. 28, pp. 1–4. https://doi.org/10.1016/S1005-0302(12)60016-4.
3. A. Yadollahi, N. Shamsaei, S.M. Thompson, A. Elwany, and L. Bian: *Int. J. Fatig.*, 2017, vol. 94, pp. 218–35. https://doi.org/10.1016/j.ijfatigue.2016.03.014.
4. H.K. Rafi, D. Pal, N. Patil, T.L. Starr, and B.E. Stucker: *J. Mater. Eng. Perform.*, 2014, vol. 23, pp. 4421–28. https://doi.org/10.1007/s11665-014-1226-y.
5. T. LeBrun, T. Nakamoto, K. Horikawa, and H. Kobayashi: *Mater. Des.*, 2015, vol. 81, pp. 44–53. https://doi.org/10.1016/j.matdes.2015.05.026.
6. R. Rashid, S.H. Masood, D. Ruan, S. Palanisamy, R.A.R. Rashid, and M. Brandt: *J. Mater. Proc. Technol.*, 2017, vol. 249, pp. 502–11. https://doi.org/10.1016/j.jmatprotec.2017.06.023.
7. S. Pasebani, M. Ghayoor, S. Badwe, H. Irrinki, and S.V. Atre: *Add. Manuf.*, 2018, vol. 22, pp. 127–37. https://doi.org/10.1016/j.addma.2018.05.011.
8. T.-H. Hsu, Y.-J. Chang, C.-Y. Huang, H.-W. Yen, C.-P. Chen, K.-K. Jen, and A.-C. Yeh: *J. Alloys Compd.*, 2019, vol. 803, pp. 30–41. https://doi.org/10.1016/j.jallcom.2019.06.289.
9. X. Wang, Y. Liu, T. Shi, and Y. Wang: *Mater. Sci. Eng. A*, 2020, vol. 792, 139776. https://doi.org/10.1016/j.msea.2020.139776.
10. M. Akita, Y. Uematsu, T. Kakiuchi, M. Nakajima, and R. Kawaguchi: *Mater. Sci. Eng. A*, 2016, vol. 666, pp. 19–26. https://doi.org/10.1016/j.msea.2016.04.042.
11. Y. Sun, R.J. Hebert, and M. Aindow: *Mater. Des.*, 2018, vol. 156, pp. 429–40. https://doi.org/10.1016/j.matdes.2018.07.015.
12. S. Vunnam, A. Saboo, C. Sudbrack, and T.L. Starr: *Add. Manuf.*, 2019, vol. 30, 100876. https://doi.org/10.1016/j.addma.2019.100876.
13. P. Leo, S. D'Ostuni, P. Perulli, M.A.C. Sastre, A.I. Fernández-Abia, and J. Barreiro: *Proc. Manuf.*, 2019, vol. 41, pp. 66–73. https://doi.org/10.1016/j.promfg.2019.07.030.
14. L. Zai, C. Zhang, Y. Wang, W. Guo, D. Wellmann, X. Tong, and Y. Tian: *Metals*, 2020, vol. 10, pp. 255–80. https://doi.org/10.3390/met10020255.
15. A.W. Wilson, J.D. Madison, and G. Spanos: *Scripta Mater.*, 2001, vol. 45, pp. 1335–40. https://doi.org/10.1016/S1359-6462(01)01137-X.

16. J. Wu, P.J. Wray, C.I. Garcia, M. Hua, and A.J. Deardo: *ISIJ Int*., 2005, vol. 45, pp. 254–62. https://doi.org/10.2355/isijinternational.45.254.
17. M. Calcagnotto, D. Ponge, and D. Raabe: *ISIJ Int*., 2012, vol. 52, pp. 874–83. https://doi.org/10.2355/isijinternationl.52.874.
18. J.-Y. Kang, S.-J. Park, and M.-B. Moon: *Micros. Microanal*., 2013, vol. 19, pp. 13–16. https://doi.org/10.1017/S1431927613012233.
19. T. Martinez Ostormujof, R.R.P.P.R. Purohit, S. Breumier, N. Gey, M. Salib, and L. Germain: *Mater. Character*., 2022, vol. 184, p. 111638. https://doi.org/10.1016/j.matchar.2021.111638.